Surface lowering of the debris-covered area of Kanchenjunga Glacier in the eastern Nepal Himalaya since 1975, as revealed by Hexagon KH-9 and ALOS satellite observations

Damodar Lamsal[a], Koji Fujita, Akiko Sakai

Graduate School of Environmental Studies, Nagoya University, Nagoya 464-8601, Japan
[a]now at: Asia Air Survey Co., Ltd., Kanagawa 215-0004, Japan

Correspondence to: Koji Fujita (cozy@nagoya-u.jp)

Abstract. This study presents the geodetic mass balance of Kanchenjunga Glacier, one of the largest debris-covered glaciers in the easternmost Nepal Himalaya, which possesses a negative mass balance of -0.18 ± 0.17 m w.e. a^{-1} for the 1975–2010 study period, estimated using digital elevation models (DEMs) generated from Hexagon KH-9 and ALOS PRISM stereo images. Accurate DEMs, with a relative uncertainty of ± 5.5 m, were generated from the intensive and manual editing of triangulated irregular network (TIN) models on a stereo MirrorTM/3D Monitor. The glacier ice-flow velocity field was also calculated using a feature-tracking method that was applied to two ALOS orthoimages taken in 2010. The elevation differences between the two DEMs highlight considerable surface lowering across the debris-covered area, and a slight thickening in the accumulation area of Kanchenjunga Glacier between 1975 and 2010. The magnitude and gradient of surface lowering are similar among the six glacier tributaries, even though they are situated at different elevations, which may reflect variations in the ice-flow velocity field. The pattern of surface lowering correlates well with the ice-flow velocity field over the debris-covered portion of the main tributary, suggesting that the glacier dynamics significantly affect surface lowering by altering the emergence velocity along the glacier, particularly in the compressive ablation area. Surface lowering patterns partially correspond to the supraglacial pond area fraction of the glacier, with enhanced surface lowering observed in areas that possess a larger pond area fraction. These findings support the hypothesis that supraglacial ponds may intensify ice wastage and play a key role in the heterogeneous surface lowering of debris-covered glaciers. The estimated mass loss of Kanchenjunga Glacier is moderate compared with other debris-covered glaciers in neighboring Himalayan regions, which may be due to the lower pond area fraction of Kanchenjunga Glacier relative to other glaciers.

1 Introduction

Glaciers in the Himalayas have been undergoing extensive and ongoing mass loss in recent decades, with the extent of this loss exhibiting a high degree of spatial heterogeneity (Fujita and Nuimura, 2011; Bolch et al., 2012; Kääb et al., 2012; Gardelle et al., 2013). There has been a growing interest in studying these changing Himalayan glaciers, but notable spatial and temporal gaps exist in existing datasets. Glaciers in the Khumbu and Langtang regions of Nepal have been frequently studied compared with other regions in the Himalayas (e.g., Nakawo et al., 1999; Bolch et al., 2011; Nuimura et al., 2011, 2012, 2017; Pellicciotti et al., 2015; Salerno et al., 2015, 2017; Ragettli et al., 2016). Khumbu Glacier is one of the most

33 extensively studied glaciers in the Himalayas, largely due to its proximity to Mt. Everest, which means the better logistical
34 facilities provide easier access to the glacier. While these repeated investigations in a particular region or on a particular
35 glacier help to strengthen our understanding of cryospheric processes, records from data-scarce regions are equally important.
36 Glaciers in the Kanchenjunga region have received little attention and are thus poorly understood, although Racoviteanu et al.
37 (2015) provided some constraints on glacier surface area changes between the 1960s and 2000s. Declassified US spy satellite
38 data (e.g., Corona KH-4 and Hexagon KH-9 stereo images) are now available, spanning the 1960s to mid-1980s timeframe
39 for many glacierized areas of the globe, which can provide valuable information about remote regions. Digital elevation
40 models (DEMs) can thus be generated from these newly accessible data sources, allowing us to investigate the multidecadal
41 mass balance of glaciers (e.g., Pieczonka et al., 2013; Pieczonka and Bolch, 2015; Maurer et al., 2016; Ragettli et al., 2016).
42 Many Himalayan glaciers are characterized by supraglacial debris cover in their ablation areas. These debris-covered glaciers
43 possess more complex and variable responses to climate change than debris-free glaciers because the debris mantle can either
44 insulate the ice or accelerate ice melting, depending on its thickness (e.g., Mattson et al., 1993; Mihalcea et al., 2008; Foster
45 et al., 2012; Juen et al., 2014). This inhomogeneous distribution of debris across debris-covered glaciers can promote
46 different rates of ice melting (e.g., Han et al., 2010; Zhang et al., 2012; Fujita and Sakai, 2014). Furthermore, the presence of
47 supraglacial ponds and ice cliffs can lead to significant and intense ice wastage (e.g., Sakai et al., 2000, 2002; Steiner et al.,
48 2015; Miles et al., 2016). However, detailed observations of ice cliffs and supraglacial ponds on debris-covered glaciers are
49 often limited to small areas of the glacier surface to elucidate the importance of these small-scale features, since they require
50 high-resolution observations. This is further complicated by the fact that many ice cliffs and supraglacial ponds on large and
51 dynamic debris-covered glaciers are either physically inaccessible or too hazardous for conducting direct measurements. This
52 study aims to provide new details on the evolution of Himalayan debris-covered glaciers by employing satellite imagery to
53 estimate the recent geodetic mass change of Kanchenjunga Glacier (27.7–27.9°N, 88.0–88.2°E; Fig. 1), a large and heavily
54 debris-covered glacier in a data-scarce region in the easternmost Nepal Himalaya. This study also aims to provide details of
55 the effects of supraglacial ponds and ice-flow velocity on the ongoing change of debris-covered glaciers.

56 **2 Data and Methods**

57 **2.1 Data**

58 Two sets of optical stereo images, obtained by Hexagon KH-9 and Advanced Land Observing Satellite–Panchromatic
59 Remote-sensing Instrument for Stereo Mapping (ALOS PRISM), are used in this study. The Hexagon KH-9 images have a
60 spatial resolution of 6–9 m and a wide geographic coverage (125 km × 250 km), with consecutive ground nadir images
61 possessing ~70% overlap (Surazakov and Aizen, 2010; Pieczonka et al., 2013). Three Hexagon KH-9 images, taken in
62 December 1975 (Table 1), were obtained from the Center for Earth Resources Observation and Science of the U.S.
63 Geological Survey, to create a DEM of Kanchenjunga Glacier and map its surface features. Three pairs of ALOS PRISM
64 images (2.5-m spatial resolution) and rational polynomial coefficient (RPC) data were also acquired from the Remote
65 Sensing Technology Center of Japan (Table 1), with the 2010 images analyzed to generate a DEM of Kanchenjunga Glacier,
66 obtain surface ice-flow velocity measurements, and map its surface features.

2.2 Glacier delineation and hypsometry

The 1975 and 2010 glacier outlines were manually delineated from the orthorectified 3-D stereoviews, which were then used to generate and edit the glacier DEMs. The identification and delineation of the glacier boundary were feasible where the images were cloud-free and possessed minimal snow cover. However, areas with poor contrast, shade, and steep snow-covered slopes, which were generally associated with topographic features (i.e., slopes and contour lines) and geomorphic features (i.e., surface roughness and crevasses), were carefully checked for proper glacier surface delineation based on our experience with remote sensing analysis in high-mountain Asia (Nuimura et al. 2015; Nagai et al. 2016; Ojha et al., 2016, 2017). The uncertainty associated with the glacier surface delineation was estimated to be ±1 pixel along its perimeter (Fujita et al., 2009; Ojha et al., 2016). The glacier was divided into 50-m elevation bands to calculate the area-weighted average and thus volume change between the two DEMs. Because the 1975 and 2010 DEMs do not cover the entire glacier, ASTER GDEM2 (Tachikawa et al., 2011) was used to calculate the glacier hypsometry, as well as the elevation of boundary between the debris-covered and debris-free glacier surfaces for the six tributaries of Kanchenjunga Glacier (labeled T1 to T6 in Fig. 1).

2.3 DEM generation from ALOS PRISM imagery

The ALOS PRISM images were processed with their RPC data, which contain information about the interior (e.g., focal length and principle point of the camera/sensor) and exterior orientations (e.g., position and tilt of the camera/sensor) of the acquired images. The joint use of stereo images and RPCs makes geometric modeling feasible, thus removing the need for ground supply points (GPCs) when generating DEMs and orthoimages. The ALOS stereo models and triangulated irregular network (TIN) model were produced from the RPC data and the Leica Photogrammetric Suite (LPS) Workstation. However, automatic terrain extraction of TIN models often contains many errors, especially in areas of highly irregular and abrupt changes in topography, which typically consist of high relief, shadowed, and low-contrast regions in the images, leading to an inaccurate terrain representation (Lamsal et al., 2011; Sawagaki et al., 2012). It is thus necessary to edit the mass points, which are the sets of vertices in XYZ-space that define the vector-based terrain surface, to obtain an accurate terrain representation. A StereoMirrorTM/3D monitor and Leica 3D TopoMouse were used for the GCP collection and terrain editing. The number of mass points defining the terrain surface depends on several factors, including the irregularity or uniformity and size of the feature, and the desired accuracy. Here we employed an average mass point density of 0.31 points per 100 m^2 (~70,000 points over 22.6 km^2), ranging from ~0.05 points per 100 m^2 on the gentle slopes around the upper boundary between debris-covered and debris-free surfaces of the glacier to ~0.8 points per 100 m^2 on the bumpy debris-covered surface of the glacier. The LPS Terrain Editor was used to edit the TIN model until the terrain representation using mass points was satisfactorily achieved, thus minimizing the errors in the DEMs. The major editing tasks included the removal of false spikes (mass points above the actual surface) and depressions (mass points below the actual surface). Then, adequate and representative mass points were placed exactly on the terrain and glacier surfaces, including supraglacial ponds and moraine ridges. The edited TIN model was then gridded into a DEM with a spatial resolution of 15 m to reduce the effect of the different levels of resolution in the TIN model (hereafter ALOS-DEM). Further details on the TIN editing and DEM creation procedures are described by Lamsal et al. (2011) and Sawagaki et al. (2012).

2.4 DEM generation from Hexagon KH-9 imagery

The Hexagon KH-9 images contain distortions from both the development and duplication of the films, as well as their long-term storage. These image distortions were corrected with the aid of the crosshairs in the images to make the images suitable for DEM extraction (Surazakov and Aizen, 2010). Since RPCs are unavailable for the Hexagon KH-9 images, GCPs were collected from the edited ALOS stereo-model, with a focus on boulders, trail intersections, and sharp notches on moraines that were clearly visible in both the ALOS PRISM and Hexagon KH-9 images. A total of 21 GCPs were extracted from the ice-free terrain surrounding Kanchenjunga Glacier (Fig. 1), with 5 GCPs (GCPv) randomly selected to independently verify the quality of the aerial triangulation (GCPv in Fig. 1). Comparison of the TIN models created with the inclusion of all 21 GCPs and with the exclusion of the 5 GCPv yielded vertical and horizontal root-mean-square errors of 4.4 m and 7.7 m, respectively, thus validating the use of the GCPs in creating the Hexagon KH-9 TIN models. The Hexagon KH-9 TIN editing and DEM generation process followed that employed to create the ALOS-DEM (Sect. 2.3). The generated Hexagon KH-9 DEM (hereafter Hex-DEM) was resampled at a spatial resolution of 15 m, following the ALOS-DEM, for consistency in comparing the DEMs.

2.5 Glacier ice-flow velocity

We calculated the surface ice-flow velocity field for Kanchenjunga Glacier using a feature-tracking method (Heid and Kääb, 2012), and then analyzed this ice-flow velocity field in combination with our DEMs to investigate the effects of topography and ice dynamics on glacier elevation changes. Orthorectified pairs of the ALOS PRISM images acquired in March 2010 and December 2010 (9-month gap) were processed using the Co-Registration of Optically Sensed Images and Correlation (COSI-Corr) algorithm, which was chosen because of its proven applications in deriving terrain displacements, including glacier ice-flow velocities, in mountainous regions (e.g., Leprince et al., 2007; Scherler et al., 2008). The COSI-Corr estimates the phase difference in the Fourier domain, and then computes the relative surface displacement between the initial (reference image) and final image (search image). The stereo images were first orthorectified and then co-registered to ensure that the corresponding pixels of the ice-free terrain in each image overlap exactly, which is required to initialize the matching process. Ice-flow velocities were computed using a correlation window of 64×64 pixels, which corresponds to a $160\,\text{m} \times 160\,\text{m}$ area, a robustness iteration of 4, and a mask threshold of 0.9 for noise reduction, following Leprince et al. (2007). To ensure the quality of the velocity map, poor matching in the surface displacement field was removed by applying a correlation threshold of 0.6, which resulted in some voids in the shaded area but also ensured that a robust ice-flow velocity map was produced (Fig. 2b). Further details on the COSI-Corr algorithm and its application to ice-flow velocity computations are described by Leprince et al. (2007) and Scherler et al. (2008). Uncertainties in the ice-flow velocity measurements were evaluated through analysis of the displacement field for the surrounding ice-free terrain possessing surface slopes gentler than 25°.

2.6 Mapping supraglacial ponds

Supraglacial ponds and ice cliffs can enhance melt on debris-covered glaciers by absorbing radiative heat and essentially producing hot spots along the glacier surface (e.g., Sakai et al., 2000, 2002; Steiner et al., 2015; Miles et al., 2016). Constraints on their spatial distribution and density are thus important in determining the role of these surface features in modifying the glacier surface. We delineated supraglacial ponds along the glacier surface during the DEM creation process

136 (Sect. 2.3 and 2.4). Supraglacial ponds appear as distinct flat terrain features in the stereo images, whereas it is difficult to

137 distinguish ice cliff and debris-covered steep slopes in the panchromatic images; we thus focused our analysis solely on the

138 distribution and evolution of supraglacial pond coverage from the satellite images. We further limited our analysis to pond

139 sizes of >0.001 km^2 (12 × 12 pixels in the ALOS images) to avoid misinterpretations due to topographic features. We also

140 performed a pond delineation analysis for Khumbu Glacier using the ALOS PRISM images taken in October 2008 (Table 1)

141 for comparison. We calculated the fraction of pixels containing ponds per 50-m elevation band, following Ragettli et al.

142 (2016). We also computed the rate of elevation change at each of the mapped ponds on a pixel-by-pixel basis between the

143 two DEMs, and constructed a polygon-based map of supraglacial ponds in 2010 to derive the average area of each pond.

144 **2.7 Geodetic mass balance and uncertainty estimates**

145 The upper accumulation area of Kanchenjunga Glacier possesses extensive snow cover, which corresponds to high brightness

146 and poor contrast regions in both the ALOS PRISM and Hexagon KH-9 images. These features precluded the creation of

147 comprehensive DEMs for the entire glacier. However, patchy DEMs were generated in the upper accumulation area from

148 nine locations that possessed better local image contrasts (hereafter named point sites, Fig. 2a). Two cases are employed to

149 estimate the rate of elevation change in the upper accumulation area above 6100 m a.s.l. where DEMs were unavailable: Case

150 1 employs the average of the rate of elevation change derived from the nine point sites (+0.01 m a^{-1}) and Case 2 uses the

151 best-fit curve for the debris-free part above 5800 m a.s.l., where positive elevation changes are observed between 5800 and

152 6100 m a.s.l. (Fig. 3a). Case 1 corresponds to the "no change assumption", with voids in the DEMs given zero values

153 (Pieczonka et al., 2013; Maurer et al., 2016), whereas Case 2 provides an alternative interpolation approach, with voids

154 replaced by the regional mean of the corresponding elevation band (Gardelle et al., 2013). However, since there are no

155 constraints on the rate of elevation change above 6100 m a.s.l., we placed an upper bound of 0.3 m a^{-1} to the curve fitting in

156 Case 2, which is based on the results of similar studies that have analyzed elevation changes for glaciers in the eastern

157 Himalayas (Nuimura et al., 2012; Maurer et al., 2016; King et al., 2017). The elevation change of the unmeasured area below

158 6100 m a.s.l. is assumed to be the same as the measured elevation change on the debris-free part. These two cases were thus

159 applied to the upper 14.3 km^2 (19% of the entire area) of Kanchenjunga Glacier to provide estimates on the surface elevation

160 changes in the accumulation area. The surface elevation change calculated from the two DEMs (dh/dt, m a^{-1}) was then

161 converted into the geodetic mass balance of the entire glacier (b_g, m w.e. a^{-1}) using the following equation:

162

163 $$b_g = \left(\sum_z \rho A_z \frac{dh_z}{dt} \right) / (\rho_w A_T), \tag{1}$$

164

165 where z is the elevation (m a.s.l.), ρ is the density of ice or firn, A_z and A_T are the areas at a given elevation (50-m elevation

166 band) and of the entire glacier (km^2), respectively, and ρ_w is the density of water (1000 kg m^{-3}). The accumulation area of

167 mountain glaciers often consists of snow and ice, whereas the ablation area is largely ice, which means that the elevation

168 change in the ablation area relates to more mass change than that in the accumulation area. Numerous mass balance studies

169 have employed a uniform ice density of ~900 kg m^{-3} for entire glaciers (e.g., Bolch et al., 2011; Nuimura et al., 2012;

170 Gardelle et al., 2013), whereas different density assumptions for the ablation and accumulation areas have been applied in

171 recent studies (e.g., Kääb et al., 2012; Pelliccicotti et al., 2015). We considered two density scenarios in this study: Scenario 1

172 assumes 900 kg m^{-3} for the entire glacier area, whereas Scenario 2 assumes 900 and 600 kg m^{-3} for the ablation and

173 accumulation areas, respectively. An equilibrium line altitude (ELA) is required for analysis of the accumulation and ablation

174 areas in Scenario 2. We assumed an ELA of 5850 m a.s.l. for the study period since the debris-free surface of Kanchenjunga

175 Glacier possesses a positive elevation change (Fig 3a). The mean of the four potential elevation change (Cases 1 and 2) and

176 density (Scenarios 1 and 2) combinations is assumed to represent the most plausible geodetic mass balance of the glacier

177 (Kääb et al., 2012).

178 The accuracy of the geodetic mass balance (σ_g) is a function of the two data sets that shape our mass balance calculation and

179 their respective uncertainties, as follows:

180

181 $$\sigma_g = \sqrt{[\sum_z \rho_i A_z(\sigma_a)^2 + \sum_z \rho A_z(\sigma_z)^2]/(\rho_w A_T)}, \tag{2}$$

182

183 where ρ_i is the ice density of 900 kg m^{-3}, σ_a is the relative vertical accuracy between the two DEMs, and σ_z is the difference

184 in the assumed elevation changes of the unmeasured upper accumulation area (Cases 1 and 2). The relative vertical accuracy

185 is evaluated as the standard deviation of the elevation difference (5.5 m and thus 0.16 m a^{-1}) of the DEMs for the ice-free

186 terrain (red polygon in Fig. 2a) and then uniformly applied to the glacier area below 6100 m a.s.l., which possesses

187 approximately continuous data coverage (Fig. 3a). We believe that the TIN editing performed on the Hexagon KH-9 and

188 ALOS PRISM images guarantees the same degree of uncertainty over the measured area, and thus assume that it can be

189 applied to the unmeasured area at the same elevation below 6100 m a.s.l. Gardelle et al. (2013) proposed employing the

190 errors in the glacier elevation change within a given elevation band as the extrapolation error. However, the bright and poorly

191 contrasted snowfields observed in our images hamper the estimation of this extrapolation error. We thus defined the error in

192 the elevation change of the upper accumulation area (σ_z) as the difference in the elevation change between Case 1 (+0.01 m

193 a^{-1}) and Case 2 (best-fit curve in Fig. 3a).

194 **3 Results**

195 The surface area of Kanchenjunga Glacier decreased from 60.5 ± 1.6 km^2 in 1975 to 59.1 ± 0.5 km^2 in 2010, revealing a 1.4 ±

196 0.1 km^2 (0.070 ± 0.006% a^{-1}) area loss over the 35-year study period. The average of the 1975 and 2010 areas (59.8 ± 1.1

197 km^2) was used to estimate the mass change of the glacier. No terminus retreat was noticeable; however, two minor tributaries

198 in the upper catchments, which were connected to the major tributaries in 1975, retreated and were disconnected by 2010 (T1

199 and T6; a close-up of the T6 change is shown in Fig. 1), leading to very small deceases in glacier size (0.15 and 0.33 km^2).

200 Considering the uncertainty in the area delineation (±0.5–1.5 km^2) and the 35-year measurement interval, our estimated

201 surface area loss of Kanchenjunga Glacier is negligible (2.3 ± 0.2%).

202 The spatial distribution of the elevation change derived from Hex-DEM and ALOS-DEM is shown in Fig.2a. DEMs are only

203 available for the lower 22.6 km^2 section (38% of the entire glacier); the debris-covered and debris-free areas are 15.0 km^2 and

204 7.6 km^2 in size, respectively. The most pronounced surface lowering was observed between 4700 and 5500 m a.s.l. (Fig. 3a).

205 The general observations are a slight lowering of the glacier near the terminus (–0.4 to 0.0 m a^{-1}), significant lowering across

206 the main ablation area (–0.7 to –1.2 m a^{-1}), and slight thickening in the uppermost debris-free areas (0.0 to +0.4 m a^{-1}),

207 although considerable spatial variability is present across the glacier.

208 Figure 2b shows the spatial distribution of the ice-flow velocity of Kanchenjunga Glacier derived from the two ALOS
209 PRISM orthoimages acquired in March 2010 and December 2010. The spatial distribution of displacement on the off-glacier
210 area, which we assume to be the uncertainty in the ice-flow velocity, and its histogram, suggest that the uncertainty in the ice-
211 flow velocity field is ~2.7 m a^{-1}. Ice-flow velocities are almost negligible in the lowermost areas, moderate in the ablation
212 areas, and fastest in the mid-glacier areas, varying from 0 to 72 m a^{-1}. However, distinct ice-flow velocities are observed
213 between the six tributaries. Furthermore, the ice-flow velocities for the main tributary (T3) show a variable pattern of speed-
214 up within the central debris-covered area (>10 m a^{-1}) that is surrounded by significantly slower ice-flow velocities on either
215 side (<10 m a^{-1}).

216 Both the number and average size of supraglacial ponds across Kanchenjunga Glacier increased from 1975 to 2010, resulting
217 in a marked increase in pond area fraction (ratio of the pond to debris-covered areas) from 0.1% to 1.1% (Table 2). Most of
218 the ponds formed in the ablation areas between 4700 and 5400 m a.s.l., coincident with the most significant lowering of the
219 debris-covered surface (Fig. 3a). We observed a significant negative correlation between the size of the 2010 supraglacial
220 ponds and the rate of elevation change, with the larger supraglacial ponds being associated with greater surface lowering
221 ($n = 35$, $r = -0.45$, $p < 0.01$; Fig. 4).

222 The geodetic mass balance of the entire glacier was estimated as follows: the measured rate of elevation change at each 50-m
223 elevation band was used for the lower ablation area (Fig. 3a), with the two assumptions of elevation change (constant value of
224 +0.01 m a^{-1} for Case 1 and the best-fit curve in Fig. 3a for Case 2) and the two density scenarios adopted for the upper
225 accumulation area above 6100 m a.s.l. (24% of the entire area) where there were no available measurements. The averaged
226 profile of elevation change for the debris-free glacier surface was then applied to rest of the unmeasured area between 5250
227 and 6100 m a.s.l. (39% of the entire area). This yielded a geodetic mass balance of Kanchenjunga Glacier ranging from –0.15
228 to –0.20 m w.e. a^{-1} for the 1975–2010 study period (–0.18 ± 0.17 m w.e. a^{-1}, Table 3). We tested the sensitivity of the
229 geodetic mass balance based on our assumptions. The density scenario does not significantly affect the resulting mass balance
230 in both cases (<0.02 m w.e. a^{-1}, Table 3). The assumption of the upper limit in Case 2 (0.3 m a^{-1}) alters the mass balance only
231 by 0.01 m w.e. a^{-1}, even if the upper limit is changed by ±0.1 m a^{-1} (gray shading in Fig. 3a). Although the mass balance
232 estimates are largely influenced by the scenario used (Cases 1 or 2), the difference in the final mass balance is only ~0.04 m
233 w.e. a^{-1} (Table 3), which is one fourth of the mass balance uncertainty (±0.17 m w.e. a^{-1}).

234 **4 Discussion**

235 **4.1 Contrasting surface lowering among tributaries**

236 Profiles of elevation change over the debris-covered and debris-free surfaces of Kanchenjunga Glacier suggest that the
237 estimated surface lowering is largely independent of elevation (Fig. 3a), in agreement with other studies across high mountain
238 Asia (e.g., Bolch et al., 2011; Pieczonka et al., 2013; Pellicciotti et al., 2015; Ragettli et al., 2016). However, distinct
239 relationships between surface lowering and elevation emerge when analyzing the surface elevation change data for each
240 tributary (Fig. 5a). Elevation gradients of surface lowering range from 1.58 to 2.36 m a^{-1} km^{-1}, with these observations
241 confined to >5500 m a.s.l. along T3 (upper T3), as opposed to the bulk of the elevation range for each of the other tributaries.
242 The boundary separating the debris-covered and debris-free areas is found at variable elevations among the tributaries,
243 suggesting that T1, upper T3, T5, and T6 largely possess debris-free surfaces, whereas T2 and T4 possess debris-covered

244 surfaces for approximately half of their respective measured sections (Fig. 5a). However, it does not appear that surface
245 lowering is affected by debris cover. Even though T5 and T6 are at lower elevations than T1, T2 and upper T3, the magnitude
246 and gradient of surface lowering is similar for all six tributaries. Since greater surface melt is expected along T5 and T6 due
247 to their lower elevations, we suggest that the higher ice-flow velocities along T5 and T6 are compensating for the anticipated
248 higher melt rates at lower elevations by increasing the emergence velocity (Fig. 5b). The convergence of ice fluxes along
249 lower T3 also affects the increased ice-flow velocities, thus suppressing the surface lowering at ~5000 m a.s.l. These
250 observations and inferences are in agreement with recent studies in the Himalayas that reported comparable surface lowering
251 trends along both debris-covered and debris-free surfaces (e.g., Kääb et al., 2012; Nuimura et al., 2012; Gardelle et al., 2013).
252 Furthermore, we observe that the debris-covered area exhibits a more negative trend (-0.51 m a^{-1}) than the debris-free ice at
253 ~5100–5850 m a.s.l. (-0.30 m a^{-1}), where both debris-covered and debris-free areas exist along Kanchenjunga Glacier (Fig.
254 3a).

255 **4.2 Influence of ice-flow velocity and supraglacial ponds on surface lowering**

256 We compare the surface lowering with ice-flow velocities and supraglacial pond area fraction at 50-m elevation bands,
257 following Ragettli et al. (2016). Figure 6 highlights the strong correlation between the surface lowering of the debris-covered
258 area of Kanchenjunga Glacier and ice-flow velocity. A strong positive correlation is observed between 4750 and 5600 m a.s.l.
259 ($n = 17, r = 0.74, p < 0.001$), indicating that slower ice-flow velocities lead to increased surface lowering. Since the glacier
260 surface is covered with debris mantle, the degree of surface melt is not a function of elevation, as is the case for debris-free
261 ice. This high correlation between surface lowering and ice-flow velocity thus suggests that the observed pattern of surface
262 lowering is affected primarily by the glacier dynamics, which experiences reduced surface lowering by increasing the
263 emergence velocity in this area of the ablation zone. However, from the glacier terminus to ~4750 m a.s.l., the opposite trend
264 is observed ($n = 5, r = -0.88, p < 0.05$), likely due to a thicker debris mantle preventing surface melt, since the slower ice-
265 flow velocities do not supply the necessary ice flux to compensate for the degree of surface melt anticipated for debris-free
266 ice. The supraglacial pond area fraction at 50-m elevation bands shows a discontinuous, but partial, effect on surface
267 lowering (Fig. 6). Four of the five elevation bands that possess a pond area fraction that is notably greater than the
268 surrounding elevation bands align with a similar marked increase in surface lowering (light blue bars in Fig. 6).
269 It should be noted that both the ice-flow velocity field and supraglacial pond coverage for Kanchenjunga Glacier were
270 obtained from the 2010 ALOS PRISM images, while the surface lowering was estimated for the 1975–2010 study period.
271 The observed surface lowering in the ablation area likely results from the imbalance between the surface negative mass
272 balance and emergence velocity, which produces a vertical upward motion due to the compressive flow regime in this region
273 (Cuffey and Paterson, 2010), such that there is a direct correlation between the ice flux gradient and surface elevation
274 changes (Nuimura et al., 2011, 2017; Vincent et al., 2017). However, since the middle section of the debris-covered area, at
275 ~5000 m a.s.l., exhibits an increase in the ice-flow velocity field where three tributaries coalesce with the main tributary T3
276 (T4, T5, and T6, Fig. 2b), the surface lowering here is suppressed by the increased ice flux and thus increased emergence
277 velocity (Sect. 4.1). These spatial patterns of the ice-flow velocity field would not change drastically though glacier thinning
278 should yield a localized slowdown in the ice-flow velocity field. Even though we do not fully understand the evolution of
279 supraglacial ponds on Kanchenjunga Glacier, it is unlikely that these ponds have persisted in the same locations for more

than three decades, which is supported by the observed increase in pond-related variables between 1975 and 2010 (Table 2). Miles et al. (2017) revealed that supraglacial ponds on Langtang Glacier tended to form in the same locations along the glacier, and concluded that the geometry of the glacier influenced this tendency. Given the distinct increase in supraglacial pond coverage along Kanchenjunga Glacier between 1975 and 2010, the increased surface lowering where there is a higher pond fraction (Fig. 4), the persistent formation of supraglacial ponds (Miles et al., 2016), and the enhanced melting effects of these ponds on debris-covered glaciers (Sakai et al., 2000; Miles et al., 2016), the observed surface lowering may have been accelerated by recent supraglacial pond formation, given the drastic increase in pond area fraction between 1975 and 2010. Continued observations of the surficial evolution of Kanchenjunga Glacier could provide an indication of whether our observations are shaped by such a recent acceleration in supraglacial pond formation.

While there are a growing number of studies that focus on surface elevation changes along Himalayan glaciers (e.g., Bolch et al., 2011; Nuimura et al., 2012; Gardelle et al., 2013; Maurer et al., 2016; Ragettli et al., 2016; King et al., 2017), few studies have attempted to infer a direct link between surface lowering, ice-flow velocity, and supraglacial ponds and cliffs (Ragettli et al., 2016; Watson et al., 2017). We thus compare our results with those of Ragettli et al. (2016) for the glaciers in the Langtang region (Fig. 7). While the relationships between surface lowering, ice-flow velocity, and supraglacial pond fraction for the glaciers in the Langtang region are not as distinct as those observed for Kanchenjunga Glacier, weak correlations between surface lowering and ice-flow velocity are observed. Langshisha and Shalbachumu glaciers show weak negative correlations between surface lowering and ice-flow velocity (Figs. 7b and 7c). There is also some indication that greater supraglacial pond fractions may enhance surface lowering (5050 m a.s.l. at Langtang Glacier, 4700 m a.s.l. at Langshisha Glacier, 4500 m a.s.l. at Shalbachumu Glacier, and 4150 m a.s.l. at Lirung Glacier; light blue bars in Fig. 7), as found along Kanchenjunga Glacier, but these observations are not robust enough to draw any conclusive links between supraglacial ponds and surface lowering in the Langtang region. Watson et al. (2017) demonstrated a strong positive correlation between cliff density and recent surface lowering at nine debris-covered glaciers in the Everest region, with a >50% likelihood of supraglacial pond and cliffs coexisting along the glacier surface. Furthermore, Salerno et al. (2017) revealed that the surface lowering of 28 glaciers in the Khumbu region was due primarily to the surface slope gradient, which exhibited strong correlations with ice-flow velocity and secondary to proglacial ponds.

4.3 Comparison of geodetic mass balance with other regions

Here we compare the geodetic mass balance of Kanchenjunga Glacier (-0.18 ± 0.17 m w.e. a^{-1}) with the results of other Himalayan glaciers that employed similar data sets (e.g., declassified Corona or Hexagon images and recent satellite images). Khumbu Glacier is the most intensively studied debris-covered glacier in the Himalayas, and is experiencing a greater degree of mass loss than Kanchenjunga Glacier, with a mass balance of -0.27 ± 0.08 m w.e. a^{-1} for the 1970–2007 period (Bolch et al., 2011). We suggest two possible causes for the mass balance differences between these two glaciers: 1) varying contributions of the accumulation and debris-covered areas; and 2) varying density of supraglacial ponds. Here we use the hypsometry of Khumbu Glacier from Nuimura et al. (2012) for comparison. If we place the ELA for both glaciers at 5850 m a.s.l., as done for Kanchenjunga Glacier in our study, then a larger portion of Kanchenjunga Glacier (54% of the entire glacier) lies above the ELA than observed on Khumbu Glacier (41%), thereby highlighting that Kanchenjunga Glacier possesses a larger accumulation area that will suppress the negative mass balance of Kanchenjunga Glacier relative to

316 Khumbu Glacier. The debris-covered area ratio of Kanchenjunga Glacier (25%, 15.0 km^2) is also much smaller than that of

317 Khumbu Glacier (40%, 8.2 km^2). This combination of a larger accumulation area and smaller debris-covered fraction for

318 Kanchenjunga Glacier would thus yield a less negative geodetic mass balance compared with Khumbu Glacier.

319 Supraglacial ponds may also play a key role in the surface lowering of the debris-covered area. We delineated supraglacial

320 ponds on Khumbu Glacier from ALOS PRISM images acquired in October 2008 for a direct comparison with our

321 Kanchenjunga Glacier results (Table 2). While the average pond size was similar on the two glaciers, all other pond-related

322 parameters are 2–4 times higher for Khumbu Glacier (Table 2). This high pond area fraction (3.7%) likely contributes to the

323 more negative geodetic mass balance of Khumbu Glacier. Recent investigations of the pond area fraction for glaciers in the

324 Langtang (Ragettli et al., 2016) and Everest regions (Watson et al., 2017) yielded pond area fractions in the 2.3%–3.3% range

325 for 4 debris-covered glaciers in the Langtang region (Ragettli et al., 2016) and 1%–7% range for 14 glaciers in the Khumbu

326 region (Watson et al., 2017). We thus conclude that the moderately negative mass balance of Kanchenjunga Glacier is

327 partially due to its smaller pond area fraction relative to other Himalayan glaciers.

328 We also compared the geodetic mass balances of debris-covered glaciers across the Himalayas (Fig. 8). The geodetic mass

329 balances of smaller glaciers (<20 km^2) possess a large degree of variability, while the four largest glaciers analyzed (>20 km^2:

330 two glaciers in Bhutan, one glacier in Langtang, and Kanchenjunga Glacier) exhibit a moderate mass loss (–0.15 to –0.24 m

331 w.e. a^{-1}) (Fig. 8). Because of their large size, the area-weighted regional means of the geodetic mass balances yield values

332 similar to those of the large glaciers (open squares in Fig. 8). The mass balance of Kanchenjunga Glacier could thus be

333 viewed as representative of the regional mass balance in the easternmost Nepal Himalaya.

334 **5 Conclusions**

335 The geodetic mass balance of Kanchenjunga Glacier, one of the largest debris-covered glaciers in the easternmost Nepal

336 Himalaya, is –0.18 ± 0.17 m w.e. a^{-1} for the 1975–2010 study period, as estimated from DEMs generated from Hexagon KH-

337 9 (1975) and ALOS PRISM (2010) stereo images. While we believe the TIN editing method employed in this study greatly

338 improves the relative accuracy of the generated DEMs (5.5 m or ~0.16 m a^{-1}), the time-consuming manual editing process

339 limited us to generating DEMs for only a single glacier. However, the DEMs in this study are valuable in validating the

340 quality of regional DEMs generated from an automated method. Another shortcoming of this study is that the generated

341 DEMs cover only 40% of the entire glacier, leading to a large uncertainty in the estimated geodetic mass balance due the high

342 brightness and poor contrast observed across the upper accumulation area in both the ALOS PRISM and Hexagon KH-9

343 images. Even with these increased uncertainties regarding the geodetic mass balance of Kanchenjunga glacier, our estimate

344 appears to be representative of the mass balance for Himalayan glaciers.

345 We observed that both the ice-flow velocity field and the presence of supraglacial ponds influenced surface lowering across

346 the debris-covered area of Kanchenjunga Glacier. Although the six tributaries are situated at different elevations, the

347 magnitude and gradient of surface lowering are similar for each, likely due to the varying ice-flow velocity field across the

348 tributaries. Furthermore, surface lowering along the main tributary (T3) is highly correlated with the ice-flow velocity field,

349 suggesting that the ice flux along T3 influences the emergence velocity and thus the degree of surface lowering, with vertical

350 uplift in the ablation area countering some of the expected surface lowering along the tributary. Surface lowering generally

351 increases along sections of the glacier that possess a larger supraglacial pond area fraction, supporting the hypothesis that

supraglacial ponds contribute to localized intense ice wastage and play a key role in the heterogeneous surface lowering of debris-covered glaciers. While supraglacial ponds seem to accelerate the surface lowering of Kanchenjunga Glacier, the entire mass loss of Kanchenjunga Glacier is moderate compared with the other debris-covered Himalayan glaciers, which may be due to the lower pond area fraction and larger accumulation area ratio of Kanchenjunga Glacier relative to other glaciers. Since similar observations from the Langtang region in Nepal have shown rather equivocal relationships between surface lowering, ice-flow velocity, and supraglacial ponds, further analyses are needed to better understand the mechanisms that influence Himalayan debris-covered glaciers.

Author contribution. D. Lamsal and A. Sakai designed the study. D. Lamsal and K. Fujita analyzed the data and wrote the manuscript with the help of A. Sakai. All authors equally contributed to the discussion of the study.

References

Bolch, T., Pieczonka, T., and Benn, D. I.: Multi-decadal mass loss of glaciers in the Everest area (Nepal Himalaya) derived from stereo imagery, The Cryosphere, 5, 349–358, doi:10.5194/tc-5-349-2011, 2011.

Bolch, T., Kulkarni, A., Kääb, A., Huggel, C., Paul, F., Cogley, J. G., Frey, H., Kargel, J. S., Fujita, K., Scheel, M., Bajracharya, S., and Stoffel, M.: The state and fate of Himalayan glaciers, Science, 336, 310–314, doi:10.1126/science.1215828, 2012.

Cuffey, K. and Paterson, W. S. B.: The Physics of Glaciers, Elsevier, Butterworth-Heineman, Burlington, MA, USA, 2010.

Foster, L. A., Brock, B. W., Cutler, M. E. J., and Diotri, F.: A physically based method for estimating supraglacial debris thickness from thermal band remote sensing data, J. Glaciol., 58(210), 677–690, doi:10.3189/2012JoG11J194, 2012.

Fujita, K. and Nuimura, T.; Spatially heterogeneous wastage of Himalayan glaciers, P. Natl. Acad. Sci. USA, 108, 14011–14014, doi:10.1073/pnas.1106242108, 2011.

Fujita, K. and Sakai, A.: Modelling runoff from a Himalayan debris-covered glacier, Hydrol. Earth Syst. Sci., 18, 2679–2694, doi:10.5194/hess-18-2679-2014, 2014.

382 Fujita, K., Sakai, A., Nuimura, T., Yamaguchi, S., and Sharma, R. R.: Recent changes in Imja Glacial Lake and its damming
383   moraine in the Nepal Himalaya revealed by in situ surveys and multi-temporal ASTER imagery, Environ. Res. Lett., 4,
384   045205, doi:10.1088/1748-9326/4/4/045205, 2009.

385 Gardelle, J., Berthier, E., Arnaud, Y., and Kääb, A.: Region-wide glacier mass balances over the Pamir-Karakoram-Himalaya
386   during 1999–2011, The Cryosphere, 7, 1263–1286, doi:10.5194/tc-7-1263-2013, 2013.

387 Han, H., Wang, J., Wei, J., and Liu, S.: Backwasting rate on debris-covered Koxkar glacier, Tuomuer mountain, China, J.
388   Glaciol., 56, 287–296, doi:10.3189/002214310791968430, 2010.

389 Heid, T., and Kääb, A.: Repeat optical satellite images reveal widespread and long term decrease in land-terminating glacier
390   speeds, The Cryosphere, 6, 467–478, doi:10.5194/tc-6-467-2012, 2012.

391 Juen, M., Mayer, C., Lambrecht, A., Han, H., and Liu, S.: Impact of varying debris cover thickness on ablation: a case study
392   for Koxkar Glacier in the Tien Shan, The Cryosphere, 8, 377-386, doi:10.5194/tc-8-377-2014, 2014.

393 Kääb, A., Berthier, E., Nuth, C., Gardelle, J., and Arnaud, Y.: Contrasting patterns of early twenty-first-century glacier mass
394   change in the Himalayas, Nature, 488, 495–498, doi:10.1038/nature11324, 2012.

395 King, O., Quincey, D. J., Carrivick, J. L., and Rowan, A. V.: Spatial variability in mass loss of glaciers in the Everest region,
396   central Himalayas, between 2000 and 2015, The Cryosphere, 11, 407–426, doi:10.5194/tc-11-407-2017, 2017.

397 Lamsal, D., Sawagaki, T., and Watanabe, T.: Digital terrain modelling using Corona and ALOS PRISM data to investigate
398   the distal part of Imja Glacier, Khumbu Himal, Nepal, J. Mt. Sci., 8, 390–402, doi:10.1007/s11629-011-2064-0, 2011.

399 Leprince, S., Barbot, S., Ayoub, F., and Avouac, J. P.: Automatic and precise orthorectification, co-registration, and subpixel
400   correlation of satellite images, application to ground deformation measurements, IEEE Trans. Geosci. Remote Sens., 45,
401   1529–1558, doi:10.1109/TGRS.2006.888937, 2007.

402 Mattson, L. E., Gardner, J. S., and Young, G. J.: Ablation on debris covered glaciers: an example from the Rakhiot Glacier,
403   Punjab, Himalaya, IAHS Publication, 218, 289–296, 1993.

404 Maurer, J. M., Rupper, S. B., and Schaefer, J. M.: Quantifying ice loss in the eastern Himalayas since 1974 using declassified
405   spy satellite imagery, The Cryosphere, 10, 2203-2215, doi:10.5194/tc-10-2203-2016, 2016.

406 Mihalcea, C., Mayer, C., Diolaiuti, G., D'Agata, C., Smiraglia, C., Lambrecht, A., Vuillermoz, E., and Tartari, G.: Spatial
407   distribution of debris thickness and melting from remote-sensing and meteorological data, at debris-covered Baltoro glacier,
408   Karakoram, Pakistan, Ann. Glaciol., 48, 49–57, doi:10.3189/172756408784700680, 2008.

409 Miles, E. S., Pellicciotti, F., Willis, I. C., Steiner, J., Buri, P., and Arnold, N. S.: Refined energy-balance modelling of a
410   supraglacial pond, Langtang Khola, Nepal, Ann. Glaciol., 57(71), 29–40, doi:10.3189/2016AoG71A421, 2016.

411 Miles, E. S., Willis, I. C., Arnold, N. S., Steiner, J., and Pellicciotti, F.: Spatial, seasonal and interannual variability of
412   supraglacial ponds in the Langtang Valley of Nepal, 1999–2013, J. Glaciol., 63, 88–105, doi:10.1017/jog.2016.120, 2017.

413 Nagai, H., Fujita, K., Sakai, A., Nuimura, T., and Tadono, T.: Comparison of multiple glacier inventories with a new
414   inventory derived from high-resolution ALOS imagery in the Bhutan Himalaya, The Cryosphere, 10, 65–85,
415   doi:10.5194/tc-10-65-2016, 2016.

416 Nakawo, M., Yabuki, H., and Sakai, A.: Characteristics of Khumbu Glacier, Nepal Himalaya: recent changes in the debris-
417   covered area, Ann. Glaciol., 28, 118–122, 1999.

Nuimura, T., Fujita, K., Fukui, K., Asahi, K., Aryal, R., and Ageta, Y.: Temporal changes in elevation of the debris-covered ablation area of Khumbu glacier in the Nepal Himalaya since 1978, Arct. Antarct. Alp. Res., 43, 246–255, doi:10.1657/1938-4246-43.2.246, 2011.

Nuimura, T., Fujita, K., Yamaguchi, S., and Sharma, R. R.: Elevation changes of glaciers revealed by multitemporal digital elevation models calibrated by GPS survey in the Khumbu region, Nepal Himalaya, 1992–2008, J. Glaciol., 58, 648–656, doi:10.3189/2012JoG11J061, 2012.

Nuimura, T., Sakai, A., Taniguchi, K., Nagai, H., Lamsal, D., Tsutaki, S., Kozawa, A., Hoshina, Y., Takenaka, S., Omiya, S., Tsunematsu, K., Tshering, P., and Fujita, K.: The GAMDAM glacier inventory: a quality-controlled inventory of Asian glaciers, The Cryosphere, 9, 849–864, doi:10.5194/tc-9-849-2015, 2015.

Nuimura, T., Fujita, K., and Sakai, K.: Downwasting of the debris-covered area of Lirung Glacier in Langtang Valley, Nepal Himalaya, from 1974 to 2010, Quatern. Int., doi:10.1016/j.quaint.2017.06.066, 2017.

Ojha, S., Fujita, K., Asahi, K., Sakai, A., Lamsal, D., Nuimura, T., and Nagai, H.: Glacier area shrinkage in eastern Nepal Himalaya since 1992 using high-resolution inventories from aerial photographs and ALOS satellite images. J. Glaciol., 62, 512-524, doi:10.1017/jog.2016.61, 2016.

Ojha, S., Fujita, K., Sakai, A., Nagai, H., and Lamsal, D.: Topographic controls on the debris-cover extent of glaciers in the Eastern Himalayas: Regional analysis using a novel high-resolution glacier inventory. Quatern. Int., doi: 10.1016/j.quaint.2017.08.007, 2017.

Pellicciotti, F., Stephan, C., Miles, E., Herreid, S., Immerzeel, W. W., and Bolch, T.: Mass-balance changes of the debris-covered glaciers in the Langtang Himal, Nepal, from 1974 to 1999, J. Glaciol., 61, 373–386, doi:10.3189/2015JoG13J237, 2015.

Pieczonka, T. and Bolch, T.: Region-wide glacier mass budgets and area changes for the Central Tien Shan between ~1975 and 1999 using Hexagon KH-9 imagery, Glob. Planet. Change, 128, 1–13, doi:10.1016/j.gloplacha.2014.11.014, 2015.

Pieczonka, T., Bolch, T., Wei, J., and Liu, S.: Heterogeneous mass loss of glaciers in the Aksu-Tarim Catchment (Central Tien Shan) revealed by 1976 KH-9 Hexagon and 2009 SPOT-5 stereo imagery, Remote Sens. Environ., 130, 233–244, doi:10.1016/j.rse.2012.11.020, 2013.

Racoviteanu, A. E., Arnaud, Y., Williams M. W., and Manley, W. F.: Spatial patterns in glacier characteristics and area changes from 1962 to 2006 in the Kanchenjunga–Sikkim area, eastern Himalaya, The Cryosphere, 9, 505–523, doi: 10.5194/tc-9-505-2015, 2015.

Ragettli, S., Bolch, T., and Pellicciotti, F.: Heterogeneous glacier thinning patterns over the last 40 years in Langtang Himal, Nepal, The Cryosphere, 10, 2075-2097, doi:10.5194/tc-10-2075-2016, 2016.

Sakai, A., Takeuchi, N., Fujita, K., and Nakawo, M.: Role of supraglacial ponds in the ablation processes of a debris-covered glacier in the Nepal Himalayas, IAHS Publication, 264, 119–130, 2000.

Sakai, A., Nakawo, M., and Fujita, K.: Distribution characteristics and energy balance of Ice cliffs on debris-covered glaciers, Nepal Himalaya, Arct. Antarct. Alp. Res., 34, 12–19, doi:10.2307/1552503, 2002.

Salerno, F., Guyennon, N., Thakuri, S., Viviano, G., Romano, E., Vuillermoz, E., Cristofanelli, P., Stocchi, P., Agrillo, G., Ma, Y., and Tartari, G.: Weak precipitation, warm winters and springs impact glaciers of south slopes of Mt. Everest (central Himalaya) in the last 2 decades (1994–2013), The Cryosphere, 9, 1229–1247, doi:10.5194/tc-9-1229-2015, 2015.

455   Salerno, F., Thakuri, S., Tartari, G., Nuimura, T., Sunako, S., Sakai, A., and Fujita, K.: Debris-covered glacier anomaly?

456   Morphological factors controlling changes in the mass balance, surface area, terminus position, and snow line altitude of

457   Himalayan glaciers, Earth Planet. Sci. Lett., 471, 19–31, doi:10.1016/j.epsl.2017.04.039, 2017.

458   Sawagaki, T., Lamsal, D., Byers, A. C., and Watanabe, T.: Changes in surface morphology and glacial lake development of

459   Chamlang South Glacier, eastern Nepal Himalaya, since 1964, Global Environ., Res., 16, 83–94, 2012.

460   Scherler, D., Leprince, S., and Strecker M. R.: Glacier-surface velocities in alpine terrain from optical satellite imagery–

461   Accuracy improvement and quality assessment, Remote Sens. Environ., 112, 3806–3819, doi:10.1016/j.rse.2008.05.018,

462   2008.

463   Steiner, J. F., Pellicciotti, F., Buri, P., Miles, E. S., Immerzeel W. W., and Reid, T. D.: Modeling ice-cliff backwasting on a

464   debris-covered glacier in the Nepalese Himalaya, J. Glaciol., 61, 889–907, doi:10.3189/2015JoG14J194, 2015.

465   Surazakov, A. B., and Aizen, V. B.: Positional accuracy evaluation of declassified Hexagon KH-9 mapping camera imagery,

466   Photogramm. Eng. Remote Sens., 76, 603–608, 2010.

467   Tachikawa T., Hato, M., Kaku, M., and Iwasaki, A.: The characteristics of ASTER GDEM version 2, Proc. IGARSS 2011

468   Symposium, Vancouver, Canada, 24–29 July 2011, 3657–3660, 2011.

469   Vincent, C., Wagnon, P., Shea, J. M., Immerzeel, W. W., Kraaijenbrink, P., Shrestha, D., Soruco, A., Arnaud, Y., Brun, F.,

470   Berthier, E., and Sherpa, S. F.: Reduced melt on debris-covered glaciers: investigations from Changri Nup Glacier, Nepal,

471   The Cryosphere, 10, 1845-1858, doi:10.5194/tc-10-1845-2016, 2016.

472   Watson, C. S., Quincey, D. J, Carrivick, J. L., and Smith, M. W.: Ice cliff dynamics in the Everest region of the Central

473   Himalaya, Geomorphol., 278, 238–251, doi:10.1016/j.geomorph.2016.11.017, 2017.

474   Zhang, Y., Fujita, K., Liu, S., Liu, Q., and Nuimura, T.: Distribution of debris thickness and its effect on ice melt at

475   Hailuogou Glacier, southeastern Tibetan Plateau, using in situ surveys and ASTER imagery, J. Glaciol., 57, 1147–1157,

476   doi:10.3189/002214311798843331, 2011.

477

478 Table 1. Details of remote sensing data used in this study to generate the digital elevation models (DEMs), map debris-
479 covered and debris-free glacier surfaces and supraglacial ponds, and compute the surface ice-flow velocity field and
480 hypsometry.

Sensor/Sensor mode	Acquisition date	Spatial resolution (m)	ID
Hexagon/Stereo	20 December 1975	7.6	DZB1211-500057L036001
			DZB1211-500057L037001
			DZB1211-500057L038001
ALOS PRISM/Stereo	9 March 2010	2.5	ALPSMF219552985
			ALPSMN219553040
			ALPSMB219553095
ALOS PRISM/Stereo	10 December 2010	2.5	ALPSMF259812985
			ALPSMN259813040
			ALPSMB259813095
ALOS PRISM/Nadir*	24 October 2008	2.5	ALPSMN045823035
			ALPSMN045823040
ASTER GDEM2^{+}	Composite since 2000	~30.0	ASTGTM2_N27E087
			ASTGTM2_N27E088
			ASTGTM2_N28E087
			ASTGTM2_N28E088

481 * For pond delineation for Khumbu Glacier; [+] For hypsometry.
482

483　Table 2. Statistics of supraglacial ponds ($\geq$1000 m^2) in the debris-covered areas of Kanchenjunga and Khumbu Glaciers.

Glacier	Date	n	A_p (km^2)	a_p (m^2)	A_d (km^2)	R_p (%)	D_p (km^{-2})
Kanchenjunga	December 1975	8	0.014	1710	15.0	0.1	0.5
Kanchenjunga	December 2010	35	0.160	4580	15.0	1.1	2.3
Khumbu	October 2008	74	0.302	4090	8.2	3.7	9.0

484　n: number of ponds, A_p: total area of ponds, a_p: average pond area, A_d: debris-covered area, R_p: pond area fraction, and D_p:

485　pond density.

486

487 Table 3. Area-weighted geodetic mass balance of Kanchenjunga Glacier for the 1975–2010 study period (m w.e. a^{-1}). Two
488 cases for the rate of elevation change, where DEMs are unavailable, and two density scenarios are assumed in our study.
489 Scenario 1 assumes a constant density of 900 kg m^{-3} for the entire glacier, whereas Scenario 2 assumes densities of 900 and
490 600 kg m^{-3} for the ablation and accumulation areas of the glacier, respectively.

dh/dt of the unmeasured area	Case 1: +0.01 m a^{-1}		Case 2: best-fit curve in Fig. 3a	
Density assumption	Scenario 1	Scenario 2	Scenario 1	Scenario 2
Mass balance	−0.19 ± 0.17	−0.20 ± 0.16	−0.15 ± 0.17	−0.17 ± 0.16
Average	−0.18 ± 0.17			

491
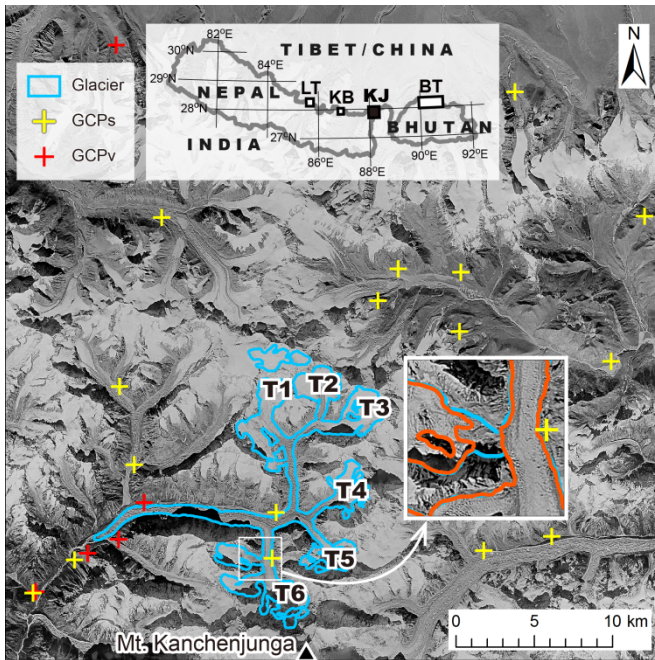
Figure 1. Outline of Kanchenjunga Glacier (blue), with 21 ground control points (GCPs), shown on a Hexagon KH-9 image taken in 1975. Five of the 21 GCPs were used to validate the accuracy of the transformation (GCPv). The major tributaries of Kanchenjunga Glacier are labeled T1 to T6. The inset map shows the location of Kanchenjunga Glacier (KJ, black box), as well as other glaciers (open boxes) in the Langtang region (LT), Khumbu region (KB), and Bhutan (BT), which were compared to this study (Fig. 7). The inset panel provides an example of the change in the glacier outline between 1975 (blue) and 2010 (orange).

Half width
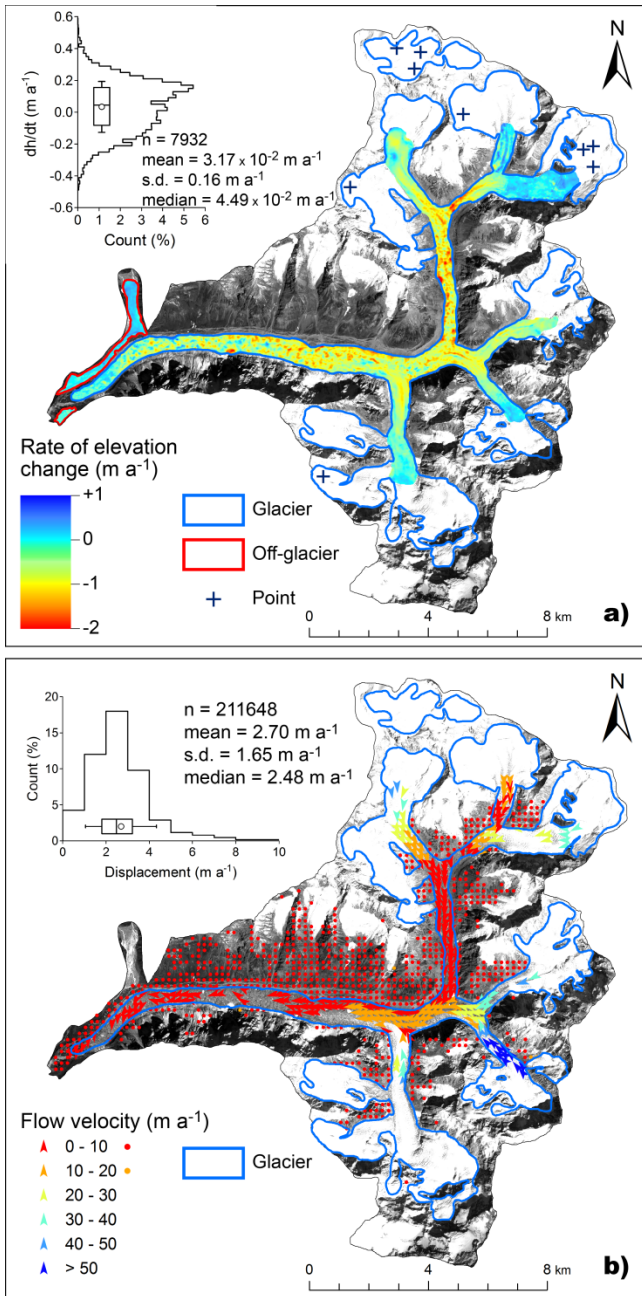
18

Figure 2. (a) Rate of elevation change for the 1975–2010 study period and (b) ice-flow velocity between March 2010 and December 2010 for Kanchenjunga Glacier. The elevation difference (a) and displacement (b) in the ice-free terrain were used to evaluate the uncertainties of the two DEMs and ice-flow velocity (inset graphs). The black crosses in (a) denote the point measurements of elevation change in the upper accumulation area. The vectors and points in (b) are depicted at a 200-m spatial interval for better visibility. The box, thick line, circle, and whiskers in the inset graphs denote the interquartile, median, mean, and one standard deviation, respectively.

Half width
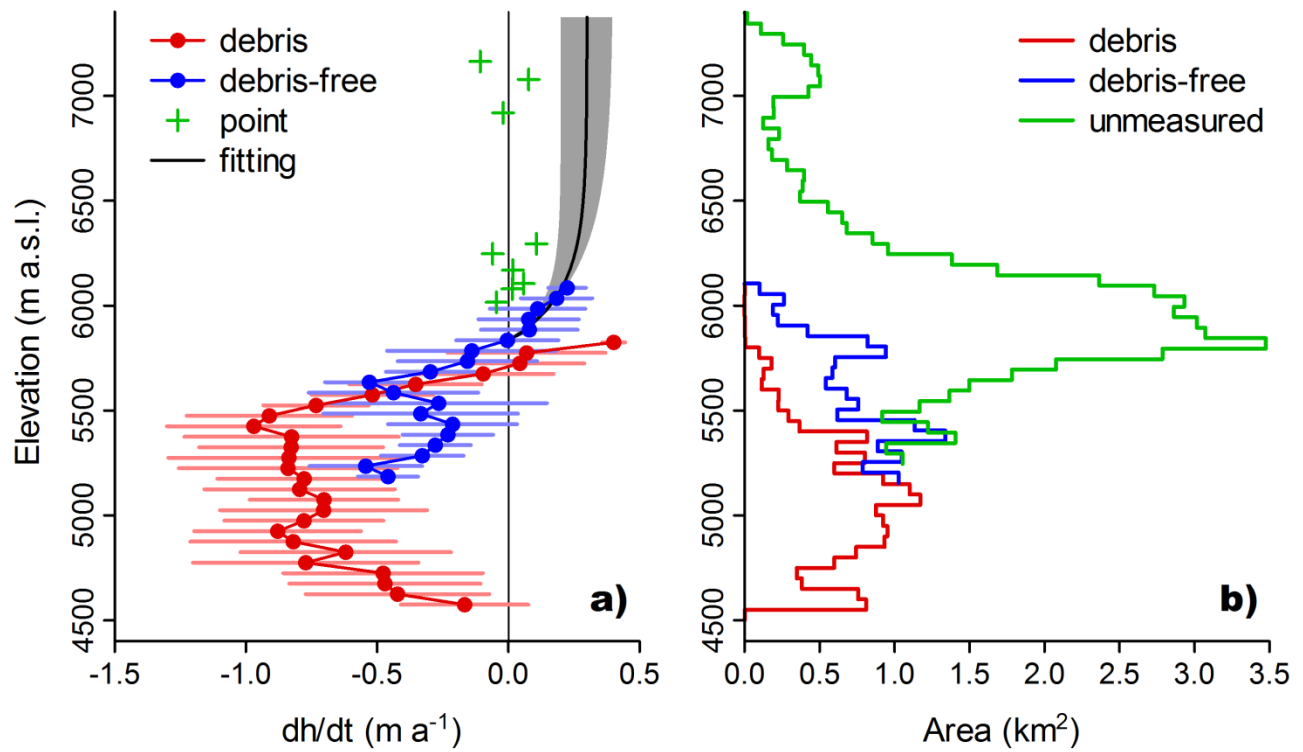
Figure 3. Elevation profiles of the (a) rate of elevation change (dh/dt) and (b) hypsometry of Kangchenjunga Glacier at 50-m elevation bands. The bars represent one standard deviation within each respective band. The green crosses and line denote the point measurements in the upper accumulation area (Fig. 2a) and the area distribution of the unmeasured part, respectively. The black line with gray shading is the best-fit curve for estimation of the elevation change in the unmeasured area (Case 2).

Full width

$n = 35$
$r = -0.45$
$p < 0.01$

517
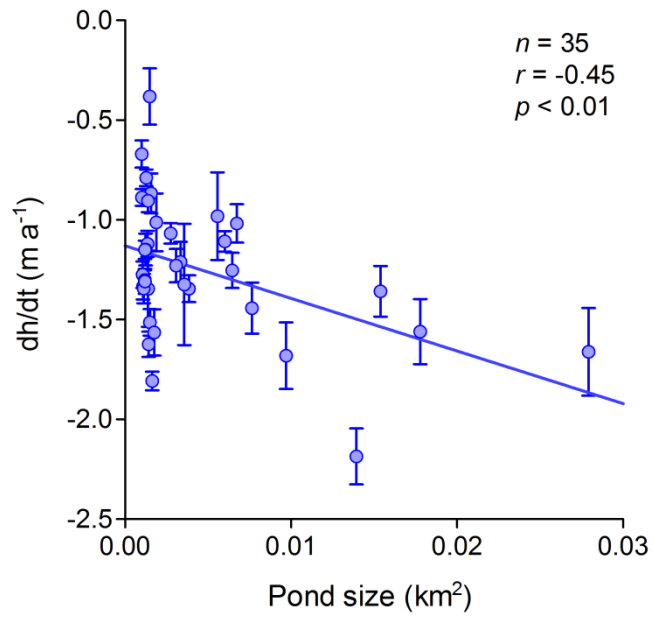
Figure 4. Rate of elevation change (dh/dt) of the supraglacial ponds observed on Kanchenjunga Glacier in 2010.
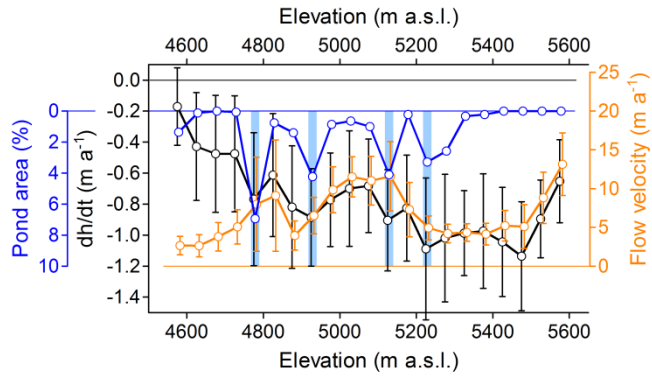
519   Half width

520
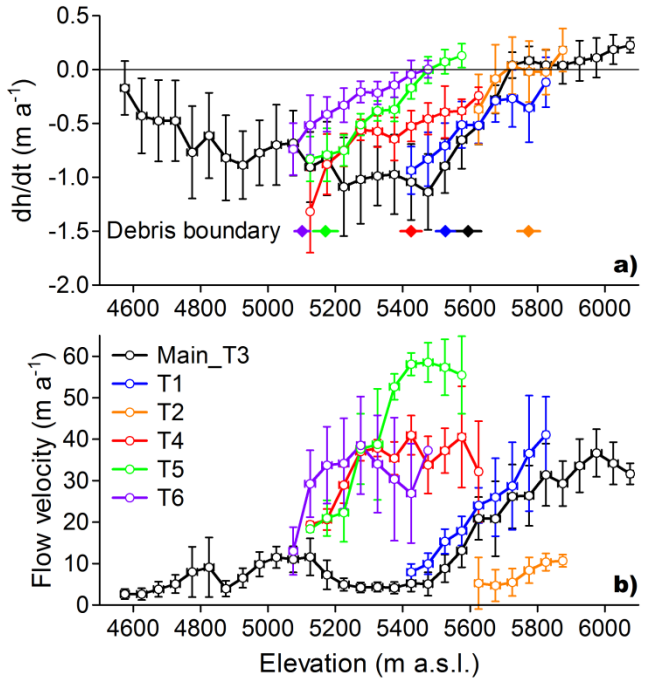
Figure 5. Elevation profiles of (a) the rate of elevation change (dh/dt) and (b) ice-flow velocity along the six tributaries of Kanchenjunga Glacier versus elevation. The tributaries are defined in Fig. 1. The elevation of the debris boundary of each tributary is indicated in (a).
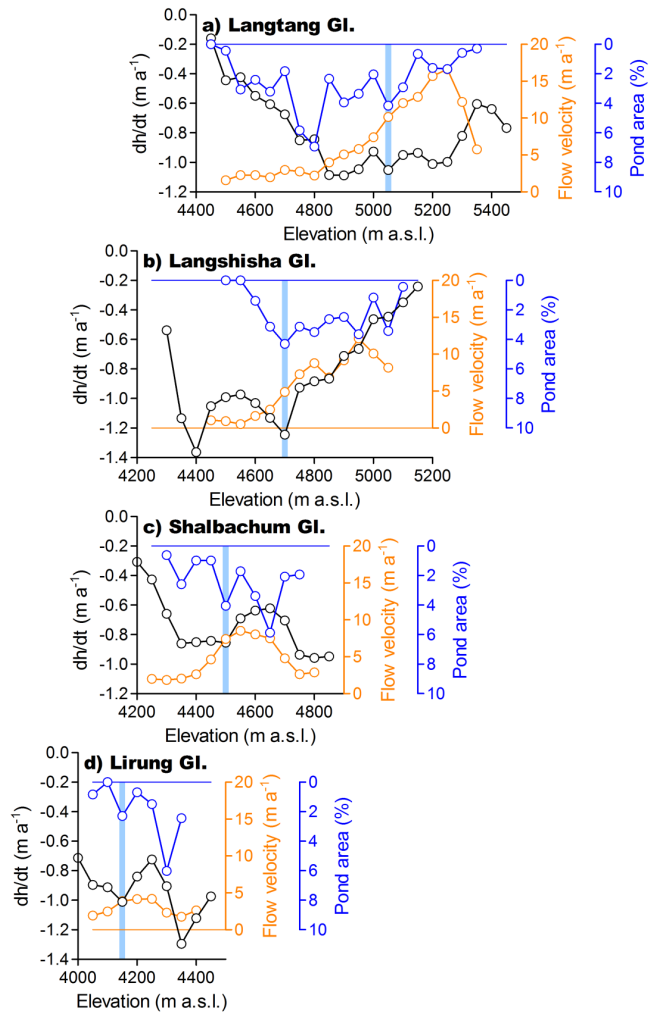
Half width

Figure 6. Elevation profiles of the change in the rate of elevation change (dh/dt, black), ice-flow velocity (orange), and supraglacial pond area fraction (blue) at 50-m elevation bands over the debris-covered area of Kanchenjunga Glacier. The light blue bars denote the peaks in supraglacial pond area fraction mentioned in the main text.

Half width

533

Figure 7. Elevation profiles of the rate of elevation change (dh/dt, black), ice-flow velocity (orange), and supraglacial pond

area (blue) versus elevation (in 50-m elevation bands) for the debris-covered area of four glaciers in the Langtang region,

Nepal Himalaya, modified from Ragettli et al. (2016). The light blue bars in each figure denote peaks in the supraglacial pond

area fraction that are mentioned in the main text.

Half width

539
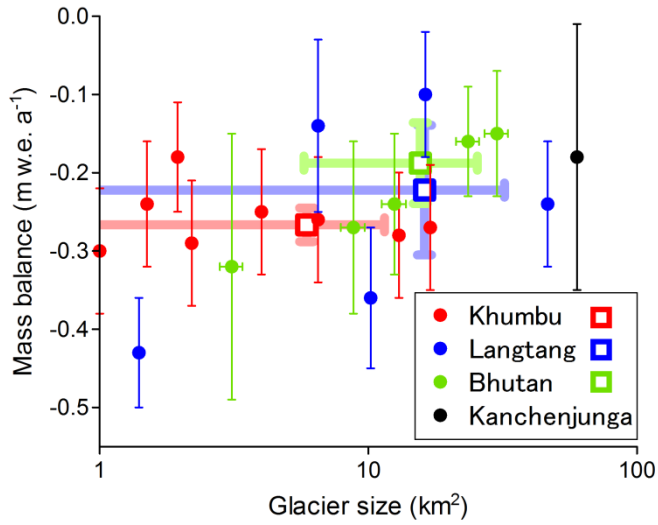
540
541 Figure 8. Geodetic mass balance of the debris-covered glaciers (solid circles) in the Himalayas, obtained from the difference
542 between two DEMs generated from declassified satellite images and more recent satellite data. The red, blue, green, and
543 black circles denote eight glaciers in the Khumbu region (Bolch et al., 2011), five glaciers in the Langtang region (Ragettli et
544 al., 2016), five glaciers in Bhutan (Maurer et al., 2016), and Kanchenjunga Glacier (this study), respectively. Open squares
545 with thick error bars are the area-weighted means and one standard deviation for the regional data sets.
546 Half width
547